

Memristor-coupled dynamics and synchronization in two bi-neuron Hopfield neural networks

Fangyuan Li(李芳苑), Haigang Tang(唐海刚), Yunzhen Zhang(张云贞), Bocheng Bao(包伯成), Hany Hassanin, and Lianfa Bai(柏连发)

Citation: Chin. Phys. B, 2025, 34 (**12**): 128701. DOI: 10.1088/1674-1056/ae101c
http://cpb.iphy.ac.cn; http://iopscience.iop.org/cpb

What follows is a list of articles you may be interested in

A physical memristor model for Pavlovian associative memory

Jiale Lu(卢家乐), Haofeng Ran(冉皓丰), Dirui Xie(谢頔睿), Guangdong Zhou(周广东), and Xiaofang Hu(胡小方)
Chin. Phys. B, 2025, 34 (**1**): 018703. DOI: 10.1088/1674-1056/ad8b37

Influences of short-term and long-term plasticity of memristive synapse on firing activity of neuronal network

Zhi-Jun Li(李志军) and Jing Zhang(张晶)
Chin. Phys. B, 2024, 33 (**12**): 128701. DOI: 10.1088/1674-1056/ad84c5

Dynamical behaviors in discrete memristor-coupled small-world neuronal networks

Jieyu Lu(鲁婕妤), Xiaohua Xie(谢小华), Yaping Lu(卢亚平), Yalian Wu(吴亚联), Chunlai Li(李春来), and Minglin Ma(马铭磷)
Chin. Phys. B, 2024, 33 (**4**): 048701. DOI: 10.1088/1674-1056/ad1483

Dynamical behavior of memristor-coupled heterogeneous discrete neural networks with synaptic crosstalk

Minglin Ma(马铭磷), Kangling Xiong(熊康灵), Zhijun Li(李志军), and Shaobo He(贺少波)
Chin. Phys. B, 2024, 33 (**2**): 028706. DOI: 10.1088/1674-1056/aceee9

Dynamics and synchronization in a memristor-coupled discrete heterogeneous neuron network considering noise

Xun Yan(晏询), Zhijun Li(李志军), and Chunlai Li(李春来)
Chin. Phys. B, 2024, 33 (**2**): 028705. DOI: 10.1088/1674-1056/ad062c

---

SPECIAL TOPIC — Biophysical circuits: Modeling & applications in neuroscience

Memristor-coupled dynamics and synchronization in two bi-neuron Hopfield neural networks

Fangyuan Li(李芳苑)[1,2], Haigang Tang(唐海刚)[3], Yunzhen Zhang(张云贞)[4], Bocheng Bao(包伯成)[3,†], Hany Hassanin[5], and Lianfa Bai(柏连发)[2]

[1] *School of Electronic Information, Nanjing Vocational College of Information Technology, Nanjing* 210023, *China*
[2] *School of Electronic and Optical Engineering, Nanjing University of Science and Technology, Nanjing* 210094, *China*
[3] *Wang Zheng School of Microelectronics, Changzhou University, Changzhou* 213159, *China*
[4] *School of Information Engineering, Xuchang University, Xuchang* 461000, *China*
[5] *School of Engineering, Technology and Design, Canterbury Christ Church University, Canterbury CT*1*QU, UK*

(Received 18 August 2025; revised manuscript received 3 October 2025; accepted manuscript online 7 October 2025)

Neural synchronization is associated with various brain disorders, making it essential to investigate the intrinsic factors that influence the synchronization of coupled neural networks. In this paper, we propose a minimal architecture as a prototype, consisting of two bi-neuron Hopfield neural networks (HNNs) coupled via a memristor. This coupling elevates the original two bi-neuron HNNs into a five-dimensional system, featuring an unstable line equilibrium set and rich dynamics absent in the uncoupled case. Our results show that varying the coupling strength and the initial state of the memristor can induce periodic, chaotic, hyperchaotic, and quasi-periodic oscillations, as well as initial-offset-regulated multistability. We derive sufficient conditions for achieving exponential synchronization and identify multiple synchronous regimes with transitions that strongly depend on the initial states. Field-programmable gate array (FPGA) implementation confirms the predicted dynamics and synchronization in real time, demonstrating that the memristive coupler enables complex dynamics and controllable synchronization in the most compact Hopfield architecture, with implications for the study of neuromorphic circuits and synchronization.

Keywords: memristor, bi-neuron Hopfield neural network (HNN), initial state dependence, synchronization

PACS: 87.19.lg, 87.19.lj, 87.19.lm, 05.45.−a

DOI: 10.1088/1674-1056/ae101c **CSTR:** 32038.14.CPB.ae101c

1. Introduction

The human brain is an extraordinarily complex organ, comprising approximately 86 billion neurons interconnected through vast synaptic networks.[1,2] Inspired by the structural and functional characteristics of biological neural systems, artificial neural networks (ANNs)[3–5] have been developed to model certain aspects of brain-like information processing. Among various types of ANNs, the Hopfield neural network (HNN) stands out as a recurrent network model with symmetric interconnections and energy-based dynamics, enabling associative memory functionality.[6,7] Today, HNNs are widely applied in combinatorial optimization,[8] encryption[9,10] and pattern recognition[11] in engineering systems.

While classical studies have primarily focused on the properties and applications of individual HNNs,[12–14] the brain's functionality fundamentally relies on the coordinated activity across different regions, enabling efficient information transmission, integration, and processing.[15] This inter-regional cooperation underlies various cognitive and behavioral functions,[16] highlighting the importance of studying interactions among neural subsystems. In recent research, various coupling schemes have been proposed to model connections between neural systems.[17–19] Among these, memristors have attracted increasing attention as particularly suitable coupling elements for neural networks, owing to their nonlinear,[20] non-volatile,[21] and signal-processing capabilities,[22] as well as their ability to emulate various electrophysiological characteristics of biological neural systems, including electromagnetic induction,[23,24] ion channel conductance,[25] and synaptic plasticity.[26] These properties make memristors highly appropriate as biologically inspired coupling devices in neural network models. In recent years, memristor-based coupling has been widely employed,[27–29] leading to the discovery of numerous intriguing dynamical behaviors, including hyperchaos,[30,31] multistability,[32–34] initial-offset boosting,[35,36] synchronization transitions[37] and chimera states.[38] Such phenomena provide valuable insights into the intricate mechanisms of neural information processing, establishing memristor-coupled neural networks as a powerful framework for exploring complex collective behaviors in neural systems.

Synchronization is essential for the proper functioning

†Corresponding author. E-mail: mervinbao@126.com

© 2025 Chinese Physical Society and IOP Publishing Ltd. All rights, including for text and data mining, AI training, and similar technologies, are reserved.

of a wide range of natural and engineered systems,[39,40] and its importance is further underscored by its implications in several brain disorders, such as Alzheimer's disease, Parkinson's disease, and epilepsy.[41] In this context, numerous studies have investigated synchronization behaviors in memristor-coupled neural networks, including full synchronization regulated by sliding mode control in a memristor-coupled model consisting of two tabu learning neurons,[42] phase synchronization between two Rulkov neurons coupled by a discrete memristor,[43] synchronization transitions induced by coupling strength in a Hindmarsh–Rose (HR)-tabu neuron network coupled via a memristor,[44] and initial-condition-induced complete synchronization in a memristor-coupled dual-neuron mapping model.[45]

Although the above studies focus on the synchronization dynamics of discrete-time memristive neural networks, continuous-time models provide a closer approximation to biological neural processes and their temporal continuity. The dynamics of the brain are inherently complex, characterized by unpredictability and sensitivity to parameters and initial conditions. This sensitivity has motivated a series of studies on memristor-coupled HNNs that specifically examine how the coupling mechanism and initial conditions influence synchronization behavior. For example, Wang *et al.*[46] proposed an eight-dimensional coupled memristive HNN model and discussed the differential effects of coupling strength on synchronization with and without time delays. Boya *et al.*[47] investigated a ring-star network of bi-neuron memristive HNNs, observing the coexistence of synchronized, cluster, and chimera states. More recently, Chen *et al.*[48] constructed a seven-dimensional memristor-coupled homogeneous HNN model and revealed synchronous transitions driven jointly by both memristor coupling strength and initial conditions.

However, the aforementioned examples, as well as most existing research, are based on high-dimensional coupled networks. In such systems, the dynamical effects and synchronization control induced by memristive coupling are often obscured by the complexity of high-dimensional interactions. In contrast, a minimal two-dimensional HNN, considered as a subsystem, offers a tractable yet nontrivial framework for clearly characterizing the intrinsic influence of memristive coupling on collective behaviors. Moreover, according to the Poincaré–Bendixson theorem, classical two-dimensional HNNs cannot exhibit chaos. Thus, what dynamical effects arise from the introduction of coupled memristors? This question motivates the present study. To the best of our knowledge, systematic investigations of memristor-coupled two-dimensional HNNs remain scarce. This work aims to address this gap by elucidating their dynamical and synchronization properties. As a prototype system, the proposed minimal network provides insights that can be generalized to larger and more complex memristive neural architectures.

The remainder of this paper is organized as follows. In Section 2, the novel MB-HNN model is constructed, and the stability of its equilibrium points is numerically analyzed. Section 3 provides a comprehensive exploration of the coupling strength-dependent dynamical behaviors and the initial-offset dynamics. In Section 4, the theoretical derivation of synchronization is presented, along with a detailed analysis of synchronous behaviors. Section 5 describes the field-programmable gate array (FPGA)-based hardware implementation and experimental measurements. Finally, conclusions are drawn in Section 6.

2. The proposed MB-HNN

This section constructs the memristor-coupled two bi-neuron Hopfield neural networks and analyzes the stability of their equilibrium set.

2.1. Description of MB-HNN

A Hopfield neural network is characterized by a set of ordinary dimensionless differential equations. For neuron i in a Hopfield neural network composed of n neurons, its dimensionless differential equation is mathematically modeled as

$$\dot{x}_i = -x_i + \sum_{j}^{n} g_{ij} \tanh x_j + I_i, \tag{1}$$

where x_i and I_i denote the membrane potential and the externally applied stimulation of neuron i, respectively; $\tanh x_j$ represents the activation function indicating the input from neuron j, and g_{ij} is the synaptic weight describing the strength of the connection between neuron i and neuron j.

Building on the bi-neuron HNN model reported in Ref. [49], which exhibits rich dynamics under external stimulation, this work constructs a coupled neural network by linking two such models via a flux-controlled memristor as proposed in Ref. [50], with $I_i = 0$ for simplicity. Since the bi-neuron HNN represents the lowest-dimensional HNN, the resulting system constitutes the minimal memristor-coupled bi-neuron Hopfield neural network (MB-HNN), whose connection graph is illustrated in Fig. 1.

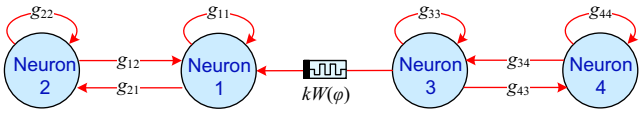


Fig. 1. Connection graph of MB-HNN.

In the MB-HNN, k denotes the memristor coupling strength between neurons 1 and 3, φ is the memristor internal state, and $W(\varphi) = \cos(\varphi)$ represents the memductance nonlinearity. Following Ref. [50], the memristor is described by

$$\begin{cases} I_{\mathrm{M}} = W(\varphi) V_{\mathrm{M}} = \cos(\varphi) \cdot V_{\mathrm{M}}, \\ \dot{\varphi} = V_{\mathrm{M}}, \end{cases} \tag{2}$$

where $I_{\rm M}$ and $V_{\rm M}$ denote the dimensionless memristor current and voltage, respectively.

Based on the connection graph shown in Fig. 1 and the coupled memristor model given in Eq. (2), the proposed MB-HNN with dimensionless variables can be mathematically expressed as

$$\begin{cases} \dot{x}_1 = -x_1 + g_{11}\tanh(x_1) + g_{12}\tanh(x_2) \\ \qquad + k\cos(\varphi)\cdot(x_1 - x_3), \\ \dot{x}_2 = -x_2 + g_{21}\tanh(x_1) + g_{22}\tanh(x_2), \\ \dot{x}_3 = -x_3 + g_{33}\tanh(x_3) + g_{34}\tanh(x_4) \\ \qquad - k\cos(\varphi)\cdot(x_1 - x_3), \\ \dot{x}_4 = -x_4 + g_{43}\tanh(x_3) + g_{44}\tanh(x_4), \\ \dot{\varphi} = x_1 - x_3. \end{cases} \tag{3}$$

Here, the dimensionless memristor voltage represents the membrane potential difference between neuron 1 and neuron 3, expressed as $V_{\rm M} = x_1 - x_3$. Thus, the MB-HNN constitutes a five-dimensional autonomous dynamical system.

2.2. Stability distribution

Denote $P = (X_1, X_2, X_3, X_4, X_5)$ as the equilibrium points of the MB-HNN. The equilibrium points can be obtained by solving the following equations:

$$\begin{cases} 0 = -X_1 + g_{11}\tanh(X_1) + g_{12}\tanh(X_2) \\ \qquad + k\cos(X_5)\cdot(X_1 - X_3), \\ 0 = -X_2 + g_{21}\tanh(X_1) + g_{22}\tanh(X_2), \\ 0 = -X_3 + g_{33}\tanh(X_3) + g_{34}\tanh(X_4) \\ \qquad - k\cos(X_5)\cdot(X_1 - X_3), \\ 0 = -X_4 + g_{43}\tanh(X_3) + g_{44}\tanh(X_4), \\ 0 = X_1 - X_3. \end{cases} \tag{4}$$

Clearly, $X_1 = X_3$, and thus $k\cos(X_5)\cdot(X_1 - X_3) = 0$. Following Ref. [49], the synaptic weights are specified as $g_{33} = g_{11} = 1.4$, $g_{34} = g_{12} = -2$, $g_{43} = g_{21} = 1.4$, and $g_{44} = g_{22} = 1.6$. Here, the bidirectional couplings are intentionally set as $g_{12} \neq g_{21}$ and $g_{34} \neq g_{43}$, reflecting the anisotropic nature of neuronal systems, since symmetric coupling strength represents only a special case in biological neural networks.[51] Consequently, the system constitutes a homogeneous neural network. Since the two subsystems share identical structures and parameters, they exhibit the same equilibrium characteristics. Taking one subsystem as an example, the equilibrium point can be obtained by solving the following equations:

$$\begin{cases} 0 = -X_1 + g_{11}\tanh(X_1) + g_{12}\tanh(X_2), \\ 0 = -X_2 + g_{21}\tanh(X_1) + g_{22}\tanh(X_2). \end{cases} \tag{5}$$

These two equations yield the solution $(0,0)$. Consequently, this five-dimensional autonomous homogeneous dynamical system possesses a line equilibrium set that can be expressed as

$$P = (0,0,0,0,\mu), \tag{6}$$

where μ is a real constant representing the initial state of the coupling memristor. In other words, the MB-HNN model has an infinite number of equilibrium points located along the φ-axis. This line equilibrium set underscores the essential role of the coupling memristor in generating complex dynamics within the MB-HNN model.

The stability of the MB-HNN model is assessed by analyzing the eigenvalues of the Jacobian matrix at the line equilibrium set P. Based on the mathematical model (3), the Jacobian matrix is derived as

$$\boldsymbol{J} = \begin{bmatrix} 0.4 + k\cos(\mu) & -2 & -k\cos(\mu) & 0 & 0 \\ 1.4 & 0.6 & 0 & 0 & 0 \\ -k\cos(\mu) & 0 & 0.4 + k\cos(\mu) & -2 & 0 \\ 0 & 0 & 1.4 & 0.6 & 0 \\ 1 & 0 & -1 & 0 & 0 \end{bmatrix}. \tag{7}$$

The corresponding characteristic polynomial is

$$P(\lambda) = \lambda(\lambda^4 + a_1\lambda^3 + a_2\lambda^2 + a_3\lambda + a_4), \tag{8}$$

where

$$\begin{aligned} a_1 &= -2 - 2k\cos(\mu), \\ a_2 &= 7.08 + 3.2k\cos(\mu), \\ a_3 &= -6.08 - 7.28k\cos(\mu), \\ a_4 &= 9.2416 + 3.648k\cos(\mu). \end{aligned}$$

Equation (8) shows that the Jacobian matrix $\boldsymbol{J}$ has one zero root and four non-zero roots. For the four non-zero roots, the Routh–Hurwitz conditions are

$$\begin{cases} (a_1a_2 - a_3)a_3 - a_1^2a_4 > 0, \\ a_i > 0, \quad (i = 1,2,3,4). \end{cases} \tag{9}$$

Satisfaction of the conditions in Eq. (9) ensures the stability of P, implying the presence of a point attractor. In contrast, if any one of the conditions is not satisfied, P becomes unstable, and periodic or chaotic behaviors may emerge. By substituting the expressions for a_i into Eq. (9), it is observed that the conditions cannot be satisfied simultaneously. For instance, although $a_1 = -2 - 2k\cos(\mu)$ can be positive for certain values of (k,μ), in those cases either a_3 becomes negative or the inequality $(a_1a_2 - a_3)a_3 - a_1^2a_4 > 0$ fails. Therefore, no combination of k and μ satisfies all the Routh–Hurwitz conditions, and the line equilibrium set P is always unstable.

To further explore and classify the unstable types, the distribution diagram of different stability types corresponding to the four non-zero eigenvalues in the μ–k parameter plane is plotted in Fig. 2, where the memristor initial state μ and coupling strength k vary within the intervals $[-2\pi, 2\pi]$ and $[-6, 6]$, respectively. As shown in Fig. 2, unstable node-focus with index-4 (UNF-4), unstable saddle-focus (USF), and unstable node-focus with index-3 (UNF-3) are represented by orange, blue, and dark blue, respectively. Specifically, the UNF-4 corresponds to four positive and zero negative real

parts (4P0N) among the non-zero eigenvalues; the USF corresponds to two positive and two negative real parts (2P2N); and the UNF-3 corresponds to three positive and one negative real parts (3P1N). For some typical k and μ selected from distinct regions, the four non-zero roots of Eq. (8) are computed and their corresponding stability types are summarized in Table 1. It is observed that these stability distributions exhibit a periodic arrangement in the μ-direction, suggesting that the system's dynamical behavior may inherit this periodic variation depending on the memristor initial state.

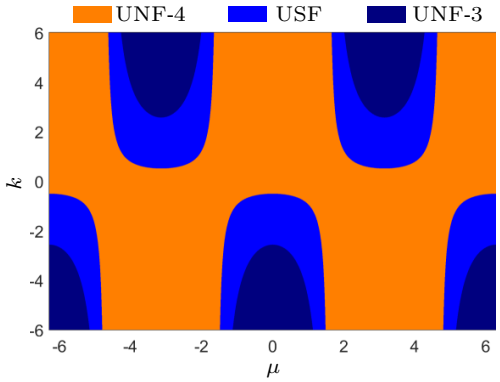


Fig. 2. The stability distribution for the line equilibrium set P in the μ–k mixed plane.

Table 1. Non-zero roots, regions and corresponding stabilities for typical memristor coupling strength k and initial condition μ.

μ, k	Non-zero roots	Stability types	Real part structure
1, 1	$0.5\pm$j1.6703, $1.0403\pm$j1.6144	UNF-4	4P0N
2, −2	$0.5\pm$j1.6703, $1.3323\pm$j1.5046	UNF-4	4P0N
0, −2	−0.2311, $0.5\pm$j1.6703, −2.7689	USF	2P2N
±3, 2	−0.2445, $0.5\pm$j1.6703, −2.7154	USF	2P2N
0, −4	0.2430, $0.5\pm$j1.6703, −7.2430	UNF-3	3P1N
±3, 5	0.3147, $0.5\pm$j1.6703, −9.2146	UNF-3	3P1N

3. Coupling dynamics of MB-HNN

In this section, we investigate dynamics dependent on the coupling strength and initial values using bifurcation diagrams and basins of attraction, and then reveal initial-offset coexisting attractors using phase plane plots. Notably, the bifurcation diagrams are generated using the MATLAB ODE45 algorithm with a fixed step size of 0.01, while the Lyapunov exponents (LEs) are computed via MATLAB using Wolf's Jacobian matrix method.

3.1. Dynamics induced by coupling strength

The coupling strength k is selected as the bifurcation parameter and varied within the range [0, 3], with the initial states of system (3) set to $(2,0,0,0,0)$. The bifurcation diagram of the state variable x_1 and the corresponding LE spectra are shown in Figs. 3(a) and 3(b), respectively.

As the coupling strength k increases within [0, 3], the MB-HNN undergoes a series of dynamic transitions. As illustrated in Fig. 3(a), the system initially maintains a stable period-1 state for $k \in [0, 0.387]$. When k enters the range [0.388, 0.554], the system transitions into a quasi-periodic regime, characterized by the presence of three zero LEs. As k increases further, the system exhibits period-3 behavior until $k = 0.689$, after which the motion becomes chaotic, followed by a return to period-1 dynamics via a chaotic crisis. A subsequent crisis occurs near $k = 1.121$, after which the system evolves from period-1 oscillations through a period-doubling bifurcation sequence into chaos again at $k = 1.534$. Notably, the system exhibits hyperchaotic behavior in the range [1.608, 1.654], where both LE_1 and LE_2 remain positive. Subsequently, the orbits return to chaos and re-enter periodic behavior at $k = 1.829$ through another chaotic crisis. The system then experiences two more transitions from period-doubling bifurcations into chaos, finally settling into periodic behavior again after k exceeds 2.392.

Therefore, system (3) displays complex dynamic behaviors under the influence of the memristive coupling, including hyperchaos, chaos, quasi-periodicity, and periodicity. Notably, hyperchaotic sequences generally offer advantages over purely chaotic sequences in specific applications, such as Wasserstein generative adversarial networks.[52]

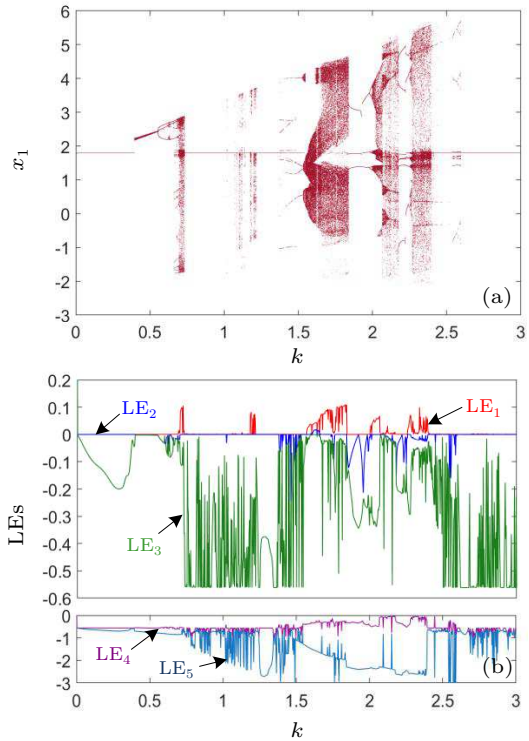


Fig. 3. Bifurcation diagram of the MB-HNN with initial states $(x_1, x_2, x_3, x_4, \varphi) = (2,0,0,0,0)$ under varying coupling strength k. (a) Bifurcation diagram of the state variable x_1. (b) Corresponding Lyapunov exponent spectra.

In order to further clarify the dynamical behavior of the system, nine representative values of k were selected, and the corresponding attractor phase portraits in the x_1–x_2 and x_3–x_4

planes were plotted, as shown in Figs. 4(a)–4(i). The results reveal a rich set of dynamical behaviors, including a period-1 limit cycle in Fig. 4(a), a quasi-periodic attractor in Fig. 4(b), hyperchaotic attractors in Fig. 4(e), chaotic attractors in Figs. 4(c)–4(f), and 4(h), and periodic attractors in Figs. 4(g) and 4(i). Notably, significant differences exist among the phase trajectories of these chaotic attractors, highlighting the diversity and complexity of the system's chaotic dynamics.

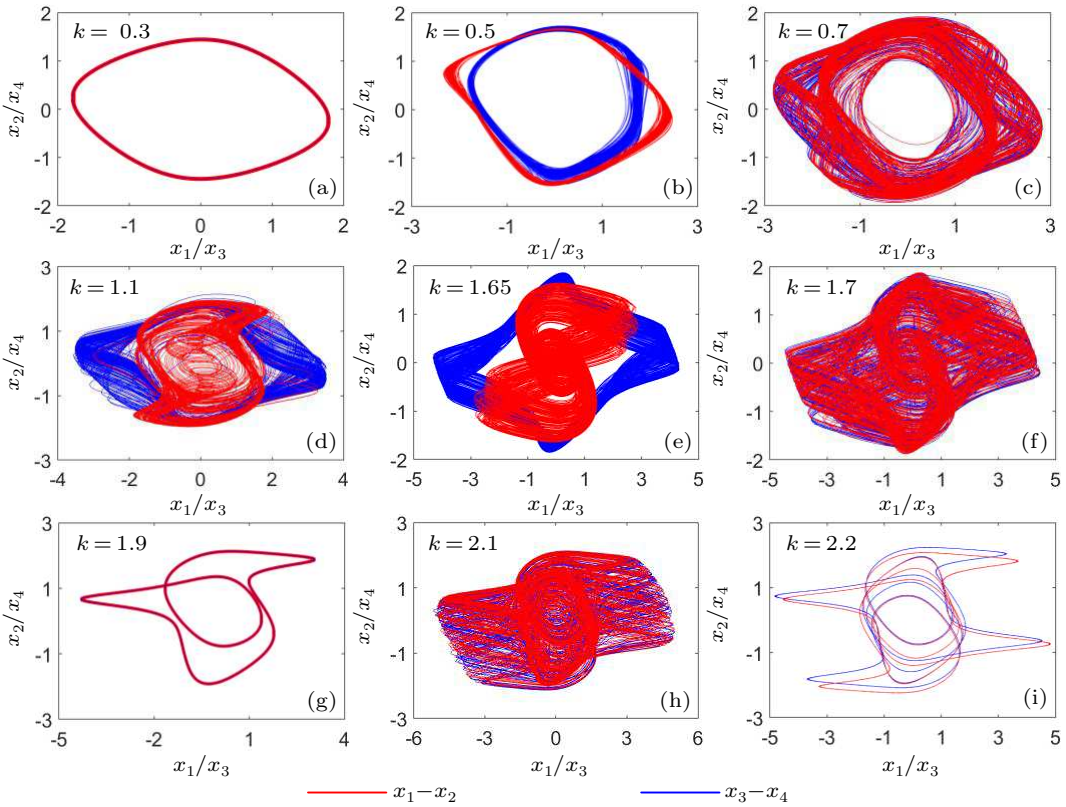


Fig. 4. Phase portraits of the MB-HNN model for different coupling strengths k with initial states $(x_1,x_2,x_3,x_4,\varphi)=(2,0,0,0,0)$ in the x_1/x_3–x_2/x_4 planes. (a) Period-1 limit cycles for $k=0.3$. (b) Quasi-periodic attractors for $k=0.5$. (c) Chaotic attractors for $k=0.7$. (d) Chaotic attractors for $k=1.1$. (e) Hyperchaotic attractors for $k=1.65$. (f) Chaotic attractors for $k=1.7$. (g) Period-2 attractors for $k=1.9$. (h) Chaotic attractors for $k=2.1$. (i) Periodic attractors for $k=2.6$.

3.2. Initial-offset dynamics

As revealed in Subsection 2.2, the MB-HNN model possesses an infinite set of equilibrium points along the φ-axis, with stability distributions forming a periodic pattern in the μ–k parameter plane. This structural periodicity implies that the system's dynamics are strongly influenced by the memristor's initial state. Based on this observation, $\varphi(0)$ is selected as the bifurcation parameter and varied within the range $[-15,15]$. The other initial states are set to $(x_1(0),x_2(0),x_3(0),x_4(0))=(2,0,0,0)$, with $k=1.8$. The bifurcation diagram of the state variable φ and the corresponding LE spectra are shown in Figs. 5(a) and 5(b), respectively.

The results demonstrate significant multistability and strong dependence on the initial state. Specifically, when $\varphi(0)$ lies within $[-1.7,1.7]$, the system exhibits chaotic behavior, as indicated by positive LEs. As $\varphi(0)$ increases to the interval $[1.7,4.6]$, the system transitions to a periodic state, with the largest LE dropping to 0. Notably, this alternating pattern of chaotic and periodic behavior repeats as $\varphi(0)$ increases or decreases in steps of 2π, maintaining the same structure. These results indicate that the system has alternating chaotic and periodic windows that are highly dependent on the initial state of the memristor, further highlighting coexisting behaviors and multistability induced by the memristor.

To further reveal the effects of initial states in the MB-HNN, the phase portraits of coexisting attractors and the corresponding local attraction basins are presented in Figs. 6(a) and 6(b), respectively. The coupling strength and the four neuron initial values are specified as $k=1.8$ and $(2,0,0,0)$. When $\varphi(0)=0,\pm2\pi,\pm4\pi$, five coexisting chaotic attractors emerge in the φ–x_1 phase plane, arranged from left to right according to increasing initial values of $\varphi(0)$, as shown in Fig. 6(a). This phenomenon suggests that by continuously increasing or decreasing $\varphi(0)$ in steps of 2π, infinitely many coexisting attractors can be obtained along the φ-axis. This initial-offset behavior represents a novel form of complex dynamics following multistability and extreme multistability.[36]

For fixed $x_2(0)=x_3(0)=x_4(0)=0$ and $k=1.8$, the local attraction basin in the $\varphi(0)$–$x_1(0)$ plane is depicted in

Fig. 6(b). The orange region represents chaotic behavior, corresponding to the chaotic attractors illustrated in Fig. 6(a). The blue region indicates period-1 limit cycle behavior; however, since its projection onto the φ–x_1 plane appears as a short line segment, it is difficult to visualize and is thus not presented in Fig. 6(a). Notably, the orange region forms a series of diagonally periodic banded structures, indicating alternating dynamical behavior along both the $\varphi(0)$- and $x_1(0)$-axes. This observation confirms that the initial-offset behaviors in the MB-HNN are highly sensitive to the system's initial states.

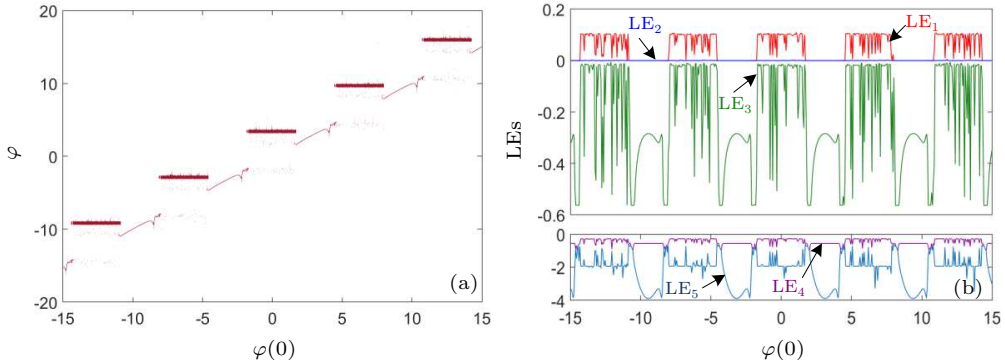


Fig. 5. Bifurcation behaviors of the MB-HNN model with respect to the memristor initial value $\varphi(0)$ for $k = 1.8$. (a) Bifurcation diagram of the state variable φ. (b) Corresponding Lyapunov exponent spectra.

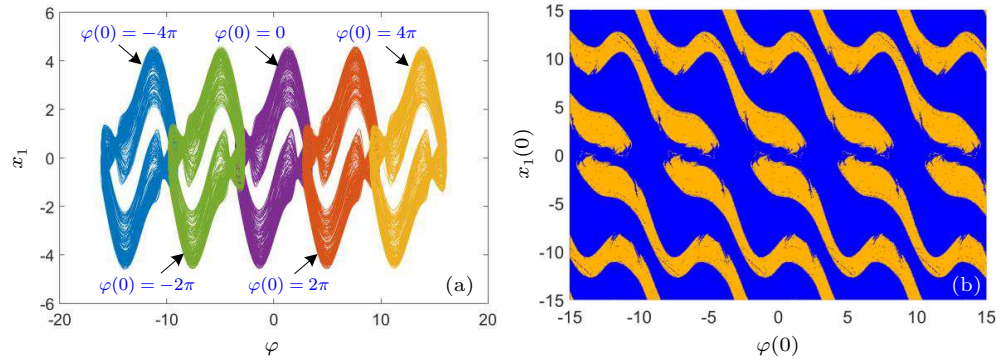


Fig. 6. Initial offset coexisting attractors and corresponding local attraction basins for $\varphi(0) = 0, \pm 2\pi$, and $\pm 4\pi$ with $k = 1.8$. (a) Phase portraits of the chaotic attractors in the φ–x_1 plane with four neuron initial values $(2,0,0,0)$. (b) Local attraction basin in the $\varphi(0)$–$x_1(0)$ plane with $x_2(0) = x_3(0) = x_4(0) = 0$.

4. Synchronization in MB-HNN

In this section, the synchronization of the MB-HNN is theoretically proven to be exponential and further examined using numerical methods. The observed synchronization behaviors include complete synchronization, lag synchronization, and phase synchronization.

4.1. Theoretical derivation of synchronicity

Define the drive variable $\boldsymbol{X} = [x_1, x_2]^{\mathrm{T}}$, the response variable $\boldsymbol{Y} = [x_3, x_4]^{\mathrm{T}}$, the coupling matrix $\boldsymbol{K} = \mathrm{diag}(k, 0)$, the error components $e_1 = x_1 - x_3$, $e_2 = x_2 - x_4$, and the error vector $\boldsymbol{e} = \boldsymbol{X} - \boldsymbol{Y} = [e_1, e_2]^{\mathrm{T}}$. The two subsystems of system (3) can then be expressed as

$$\dot{\boldsymbol{X}} = f(\boldsymbol{X}) + \boldsymbol{K}\cos(\varphi)\cdot(\boldsymbol{X} - \boldsymbol{Y}),$$

$$\dot{\boldsymbol{Y}} = f(\boldsymbol{Y}) - \boldsymbol{K}\cos(\varphi)\cdot(\boldsymbol{X} - \boldsymbol{Y}). \tag{10}$$

The nonlinear functions $f(\boldsymbol{X})$ and $f(\boldsymbol{Y})$ are

$$f(\boldsymbol{X}) = \begin{bmatrix} -x_1 + g_{11}\tanh(x_1) + g_{12}\tanh(x_2) \\ -x_2 + g_{21}\tanh(x_1) + g_{22}\tanh(x_2) \end{bmatrix},$$
$$f(\boldsymbol{Y}) = \begin{bmatrix} -x_3 + g_{33}\tanh(x_3) + g_{34}\tanh(x_4) \\ -x_4 + g_{43}\tanh(x_3) + g_{44}\tanh(x_4) \end{bmatrix}. \tag{11}$$

Consequently, the error system corresponding to Eq. (3) is formulated as

$$\dot{\boldsymbol{e}} = f(\boldsymbol{X}) - f(\boldsymbol{Y}) + 2\boldsymbol{K}\cos(\varphi)\boldsymbol{e}. \tag{12}$$

Based on the definitions in Eq. (7), and noting that $g_{33} = g_{11}$, $g_{34} = g_{12}$, $g_{43} = g_{21}$, and $g_{44} = g_{22}$, we derive

$$\begin{aligned} f(\boldsymbol{X}) - f(\boldsymbol{Y}) &= \begin{bmatrix} -(x_1 - x_3) + g_{11}(\tanh(x_1) - \tanh(x_3)) + g_{12}(\tanh(x_2) - \tanh(x_4)) \\ -(x_2 - x_4) + g_{21}(\tanh(x_1) - \tanh(x_3)) + g_{22}(\tanh(x_2) - \tanh(x_4)) \end{bmatrix} \\ &= -\boldsymbol{e} + \boldsymbol{G}\cdot\begin{bmatrix} \tanh(x_1) - \tanh(x_3) \\ \tanh(x_2) - \tanh(x_4) \end{bmatrix} = -\boldsymbol{e} + \boldsymbol{G}\cdot\boldsymbol{\Delta}\tanh, \end{aligned} \tag{13}$$

where $\boldsymbol{G}=\begin{bmatrix} g_{11} & g_{12} \\ g_{21} & g_{22} \end{bmatrix}$ and $\boldsymbol{\Delta}\tanh=\begin{bmatrix} \tanh(x_1)-\tanh(x_3) \\ \tanh(x_2)-\tanh(x_4) \end{bmatrix}$.

Clearly, $\boldsymbol{e}=0$ serves as an equilibrium point of the error system (12). This leads to the following theorem.

Theorem 1 Let the coupling strength k and the memristor initial state φ_0 satisfy

$$2k\cos(\varphi)<1-\|\boldsymbol{G}\|, \tag{14}$$

then in the error system (12), the zero solution is exponentially asymptotically stable, and system (3) achieves complete synchronization.

Proof Consider the Lyapunov function candidate $V(t,\boldsymbol{e})=0.5\boldsymbol{e}^{\mathrm{T}}\boldsymbol{e}$ for the error system (12). Its time derivative along the system trajectories is

$$\begin{aligned}\dot{V}(t,\boldsymbol{e}) &= 0.5\dot{\boldsymbol{e}}^{\mathrm{T}}\boldsymbol{e}+0.5\boldsymbol{e}^{\mathrm{T}}\dot{\boldsymbol{e}}\\ &= 0.5[f(\boldsymbol{X})-f(\boldsymbol{Y})]^{\mathrm{T}}\boldsymbol{e}+\cos(\varphi)\boldsymbol{e}^{\mathrm{T}}\boldsymbol{K}\boldsymbol{e}\\ &\quad +0.5\boldsymbol{e}^{\mathrm{T}}[f(\boldsymbol{X})-f(\boldsymbol{Y})]+\cos(\varphi)\boldsymbol{e}^{\mathrm{T}}\boldsymbol{K}\boldsymbol{e}\\ &= -\boldsymbol{e}^{\mathrm{T}}\boldsymbol{e}+\boldsymbol{G}\cdot\boldsymbol{\Delta}\tanh\cdot\boldsymbol{e}+2k\cos(\varphi)\boldsymbol{e}^{\mathrm{T}}\boldsymbol{e}. \end{aligned}\tag{15}$$

Since $\tanh'(x)=1-\tanh^2(x)\le 1$, we have $\tanh(x_1)-\tanh(x_3)=\tanh'(\xi)\cdot(x_1-x_3)$, $\tanh(x_2)-\tanh(x_4)=\tanh'(\varsigma)\cdot(x_2-x_4)$, for $\xi\in(x_1,x_3)\cup(x_3,x_1)$ and $\varsigma\in(x_2,x_4)\cup(x_4,x_2)$. Therefore, $\|\boldsymbol{\Delta}\tanh\|\le\|\boldsymbol{e}\|$.

It follows that

$$\begin{aligned}\dot{V}(t,\boldsymbol{e}) &\le -\|\boldsymbol{e}\|^2+\|\boldsymbol{G}\|\cdot\|\boldsymbol{e}\|^2+2k\cos(\varphi)\|\boldsymbol{e}\|^2\\ &= (-1+\|\boldsymbol{G}\|+2k\cos(\varphi))\|\boldsymbol{e}\|^2. \end{aligned}\tag{16}$$

Thus,

$$\begin{aligned}V(t,\boldsymbol{e}) &\le V[t_0,\boldsymbol{e}(t_0)]\\ &\quad\times\exp\{2[-1+\|\boldsymbol{G}\|+2k\cos(\varphi)](t-t_0)\}. \end{aligned}\tag{17}$$

If $-1+\|\boldsymbol{G}\|+2k\cos(\varphi)<0$, $V(t,\boldsymbol{e})$ approaches zero as $t\to\infty$, implying that $\boldsymbol{e}=0$ is exponentially asymptotically stable and complete synchronization occurs in system (3).

Remark 1 According to the fifth equation in system (3), the memristor variable φ can be expressed as

$$\varphi=\varphi_0+\int_0^t e_1\,\mathrm{d}\tau. \tag{18}$$

This indicates that the synchronization condition in Eq. (14) depends not only on the synaptic weights $\boldsymbol{G}$ and coupling strength k, but also on the initial state φ_0 of the coupling memristor.

4.2. Normalized mean synchronization error

The synchronization error between the two subsystems is quantitatively evaluated using the normalized mean synchronization error,[53] denoted by E, which is defined as

$$E=\frac{1}{N}\sum_{n=1}^{N}\frac{\sqrt{(x_1(n)-x_3(n))^2+(x_2(n)-x_4(n))^2}}{\sqrt{x_1(n)^2+x_2(n)^2+x_3(n)^2+x_4(n)^2}}, \tag{19}$$

where n denotes a natural number, and $x_j(n)$ and $y_j(n)$ are the n-th sampled values of the motion trajectories over a given time interval. For illustrative purposes, the interval [500, 1000] is used with a step size of 0.1, resulting in a total of $N=5000$ samples. According to Eq. (19), an E value of 0 corresponds to complete synchronization between the two subsystems, whereas a value approaching 1.414 indicates complete inverse synchronization.

The initial states of the two subsystems are set to $(x_1(0),x_2(0),x_3(0),x_4(0))=(2,0,0,0)$. By varying the memristor coupling strength k within [0, 3] and the initial value $\varphi(0)$ within $[-3, 3]$, the distribution of E is illustrated in Fig. 7(a). As shown, the blue regions where E approaches zero correspond to complete synchronization. The green-to-yellow regions with intermediate E values indicate partial or incomplete synchronization, while the dark red regions, where E approaches 1.414, indicate inverse synchronization. As the coupling strength k increases, the system exhibits transitions across asynchronization, synchronization, and inverse synchronization, demonstrating a rich variety of dynamical synchronization states.

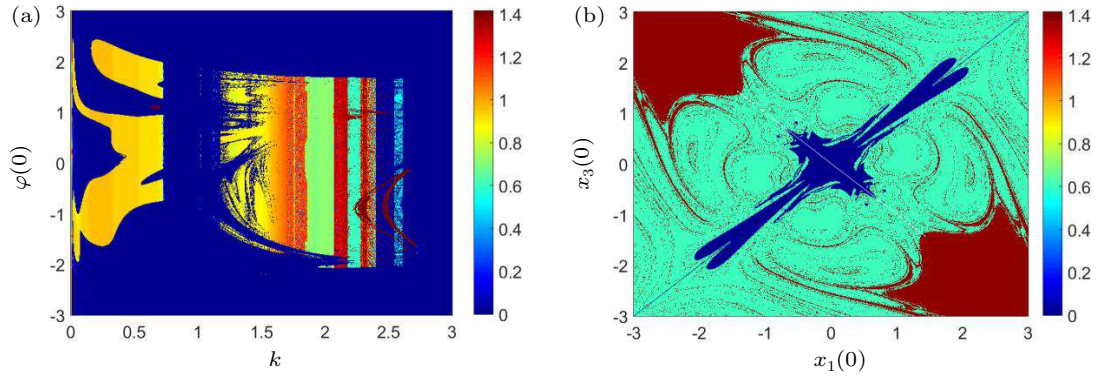


Fig. 7. Two-dimensional NMSE distributions under different parameter settings. (a) NMSE in the k–$\varphi(0)$ plane with four neuron initial conditions $(2,0,0,0)$. (b) NMSE in the $x_1(0)$–$x_3(0)$ plane with $k=2.2$ and $\varphi(0)=x_2(0)=x_4(0)=0$.

In addition, to investigate the dependence of synchronization on the initial states of the neurons, the memristor coupling strength is set to $k = 2.2$ and the memristor initial value to $\varphi(0) = 0$. With $x_2(0) = x_4(0) = 0$, the initial states $x_1(0)$ and $x_3(0)$ are varied independently within the range $[-3, 3]$. The corresponding values of E are illustrated in Fig. 7(b). Different types of synchronization behaviors are indicated using the same color scheme as in Fig. 7(a): blue for complete synchronization, green-yellow for partial/asynchronous states, and red for inverse synchronization.

As shown in Fig. 7(b), the distribution of E exhibits a symmetric pattern. The narrow diagonal blue region corresponds to strong synchronization, where E approaches zero. At the two ends along the sub-diagonal, where the difference between $x_1(0)$ and $x_3(0)$ is large, inverse synchronization occurs. The remaining parameter regions mainly correspond to asynchronous behavior. These results further confirm that both the memristor coupling strength and the initial states of the neurons play crucial roles in determining the synchronization properties of the MB-HNN.

4.3. Complete synchronization

Based on the NMSE distribution in the k–$\varphi(0)$ plane shown in Fig. 7(a), four representative pairs of $(k, \varphi(0))$ values are selected to further illustrate the synchronization behavior. For each pair, the time-domain waveforms of x_1 and x_3, as well as their phase trajectories in the x_1–x_3 plane, are plotted in Fig. 8.

As shown in Fig. 8(a), for $k = 1.6$ and $\varphi(0) = 0$, both subsystems exhibit chaotic spiking, but the trajectories of x_1 and x_3 differ, and the phase portrait in the x_1–x_3 plane is not a straight line, indicating asynchronization. For $k = 1.6$ and $\varphi(0) = 0.5$, the system still shows chaotic spiking and remains unsynchronized, as depicted in Fig. 8(b). Interestingly, the waveform of x_1 in case (b) mirrors x_3 in case (a), and vice versa; the corresponding x_1–x_3 trajectory is a rotated version of that in (a). In contrast, for $k = 1$ and $\varphi(0) = 1$, Fig. 8(c) shows that the two subsystems achieve complete synchronization, exhibiting periodic spiking, with the x_1–x_3 trajectory forming a straight line at 45 degrees. Finally, for $k = 2.3$ and $\varphi(0) = 1$, Fig. 8(d) demonstrates inverse synchronization: the two subsystems fire periodic spikes in opposite directions, and the trajectory forms a straight line at -45 degrees.

Next, by fixing $k = 2.2$ and referring to the NMSE distribution in the $x_1(0)$–$x_3(0)$ plane shown in Fig. 7(b), four representative initial state pairs $(x_1(0), x_3(0))$ are selected. The corresponding time-domain waveforms and phase trajectories are plotted in Fig. 9.

When $(x_1(0), x_3(0)) = (0, -1)$, i.e., the system is initialized as $(0, 0, -1, 0, 0)$, both x_1 and x_3 exhibit chaotic spiking, and the x_1–x_3 trajectory confirms asynchronization, as shown in Fig. 9(a). For $(x_1(0), x_3(0)) = (2, 3)$, the system also displays chaotic spiking, with slightly different waveforms and trajectories compared to case (a), as illustrated in Fig. 9(b). When $x_1(0) = x_3(0) = 1$, identical initial values lead to complete synchronization, demonstrated by overlapping time-domain waveforms and a 45-degree line in the x_1–x_3 plane, as shown in Fig. 9(c). Finally, for $(x_1(0), x_3(0)) = (2, -2)$, Fig. 9(d) shows that the opposite initial values result in inverse synchronization.

In summary, the synchronization behavior in the MB-HNN strongly depends on both the memristor coupling strength and the initial states of the neurons. Analogously, in biological neural systems, perturbations to connectivity or instantaneous neural states may induce synchronization, which is often associated with neurological disorders.

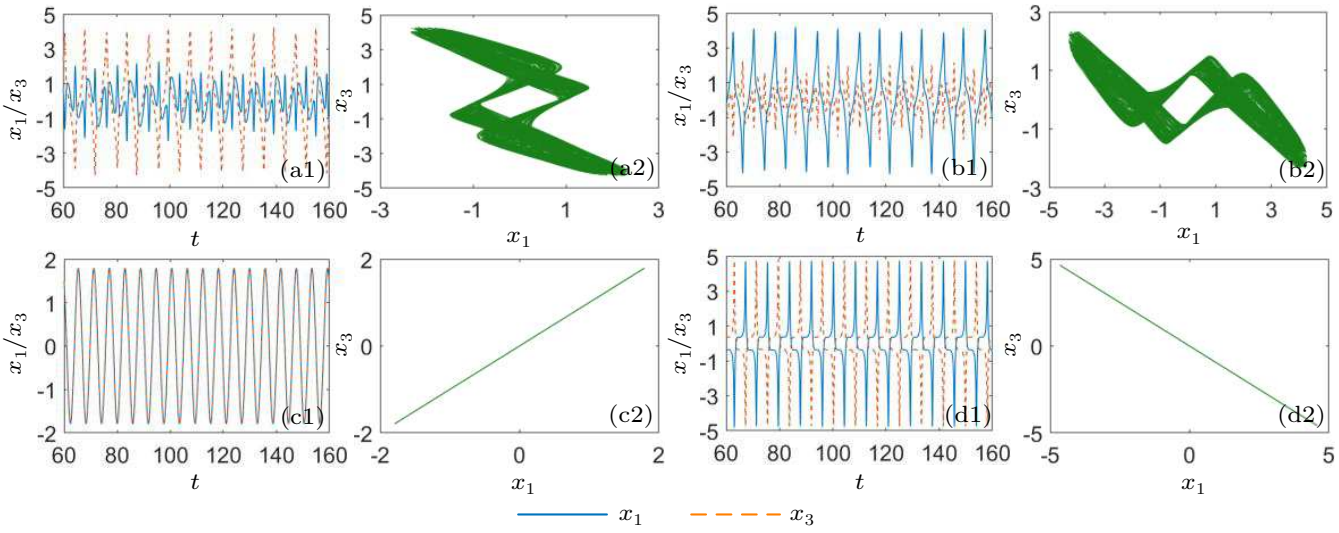


Fig. 8. Synchronous behaviors of the MB-HNN for different k and $\varphi(0)$ values with four neuron initial states $(2, 0, 0, 0)$. (a1)–(d1) Time sequences of chaotic or periodic spiking; (a2)–(d2) corresponding phase portraits in the x_1–x_3 plane. (a) $k = 1.6$, $\varphi(0) = 0$; (b) $k = 1.6$, $\varphi(0) = 0.5$; (c) $k = 1$, $\varphi(0) = 1$; (d) $k = 2.3$, $\varphi(0) = 1$.

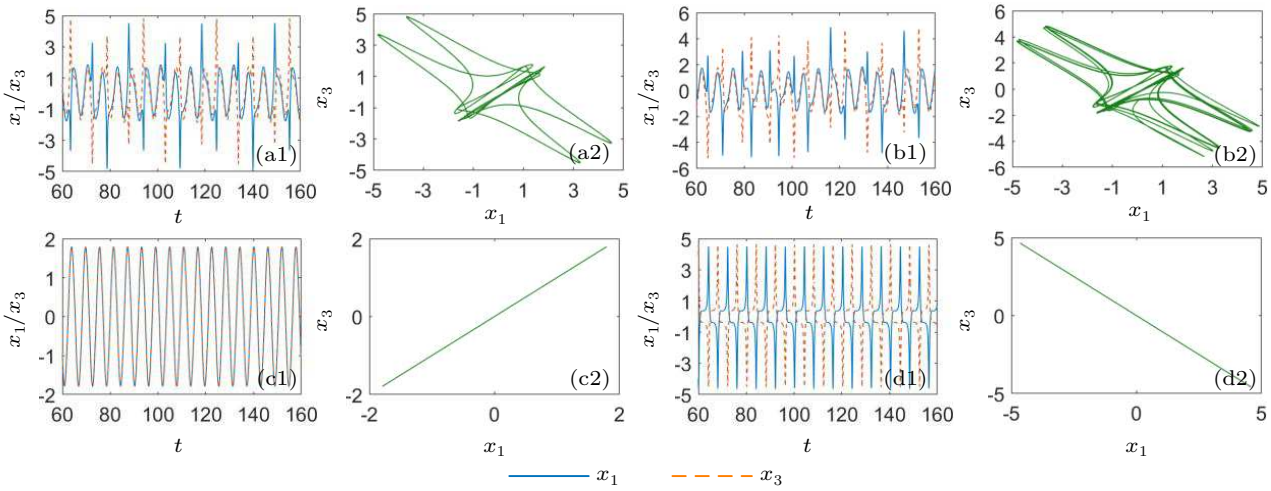


Fig. 9. Synchronous behaviors of the MB-HNN for different $x_1(0)$ and $x_3(0)$ values with $k = 2.2$, $\varphi(0) = 0$, and $x_2(0) = x_4(0) = 0$. (a1)–(d1) Time sequences of chaotic or periodic spiking; (a2)–(d2) corresponding phase portraits in the x_1–x_3 plane. (a) $x_1(0) = 0$, $x_3(0) = -1$; (b) $x_1(0) = 2$, $x_3(0) = 3$; (c) $x_1(0) = 1$, $x_3(0) = 1$; (d) $x_1(0) = 2$, $x_3(0) = -2$.

4.4. Lag synchronization

In brain networks, lag synchronization may reflect altered signal propagation pathways or reduced conduction efficiency, as observed in neurological disorders such as epilepsy.[41] This delayed coordination can be more difficult to detect than perfect synchronization, potentially masking early signs of network dysfunction.

To quantitatively analyze this lagging behavior, a similarity function[54] is introduced to evaluate the correlation between the electrical activities of the two subsystems. Its mathematical form is given by

$$S^2(\tau) = \frac{\langle [\varphi_2(t+\tau) - \varphi_1(t)]^2 \rangle}{\sqrt{\langle \varphi_1^2(t) \rangle \langle \varphi_2^2(t) \rangle}}. \tag{20}$$

When $S(\tau)$ approaches zero, it indicates that the firing behaviors of the two subsystems are identical, with a time lag of τ between them.

Corresponding to Fig. 4(g), for the initial state $(2,0,0,0,0)$ and a coupling strength of $k = 1.9$, the phase portraits in the x_1–x_3 and x_2–x_4 planes appear completely overlapped. However, as shown in Fig. 7(a), the system does not achieve complete synchronization.

Under these conditions, the similarity function $S(\tau)$ of system (3) is plotted in Fig. 10. It is observed that $S(\tau) = 0$ at $\tau = 6.2$, and again at $\tau = 18.6$, indicating that the two subsystems exhibit lag synchronization with a periodic time shift.

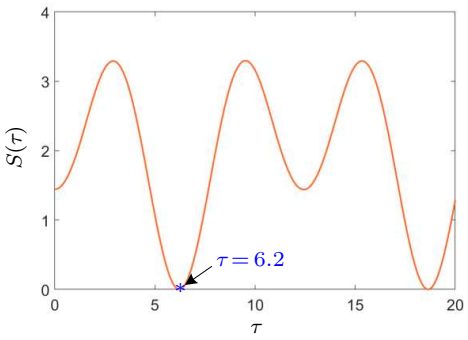


Fig. 10. Time of evolutions of similar function $S(\tau)$ for $k = 1.9$.

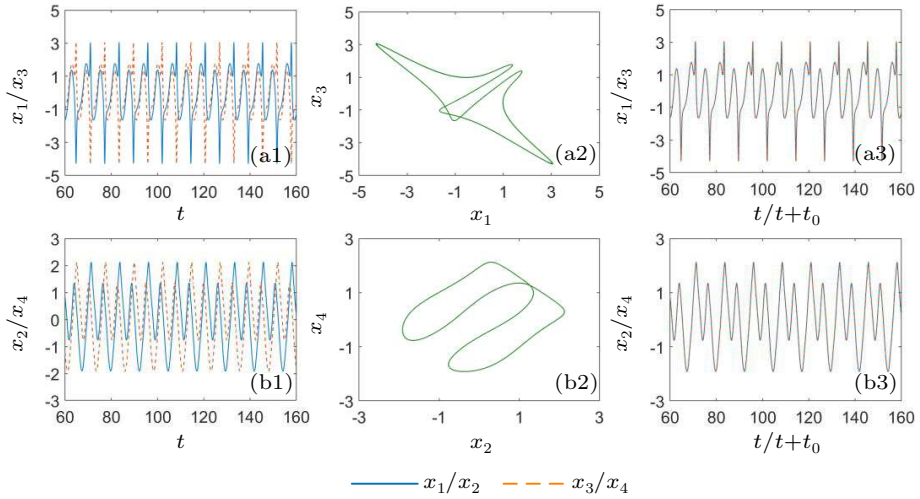


Fig. 11. Lag synchronization behaviors for $k = 1.9$ with initial states (2, 0, 0, 0, 0). (a1), (a3), (b1), and (b3) show the time sequences of spiking; (a2) and (b2) present the phase portraits in the x_1–x_3 and x_2–x_4 planes, respectively. (a) Trajectories of x_1 and x_3; (b) trajectories of x_2 and x_4.

Figures 11(a1) and 11(b1) present the time series of x_1 and x_3, as well as x_2 and x_4. The corresponding phase portraits in the x_1–x_3 and x_2–x_4 planes are shown in Figs. 11(a2) and 11(b2), revealing asynchronization between the subsystems. However, when $x_3(t)$ and $x_4(t)$ are shifted relative to $x_1(t)$ and $x_2(t)$ by a delay of $t_0 = 124$, which corresponds to 6.2 time units with a step size of 0.05, the respective trajectories become completely overlapped, as illustrated in Figs. 11(a3) and 11(b3). This observation further confirms the presence of lag synchronization in the system.

4.5. Phase synchronization

While lag synchronization captures delayed alignment of neural activities, phase synchronization reflects the preservation of phase relationships between oscillations, independent of amplitude similarity.[55] Following the approach in Refs. [55,56], the phase of a chaotic or periodic trajectory can be defined as

$$\theta(t) = 2\pi n + 2\pi \frac{t - t_n}{t_{n+1} - t_n}, \quad (t_n < t < t_{n+1}), \tag{21}$$

where t_n denotes the instant of the n-th intersection of the trajectory with a suitable Poincaré section. Each successive crossing corresponds to a 2π phase increment, and intermediate values are obtained through linear interpolation. Phase synchronization between the two coupled subsystems is then determined from the difference in their phases.

The phase difference $\Delta\theta(t) = \theta_{x_1}(t) - \theta_{x_3}(t)$ is computed from the x_1 and x_3 components of system (3) for further analysis. For different values of the coupling strength k, the time-domain sequences are plotted in Fig. 12. These three cases correspond to the phase portraits shown earlier in Figs. 4(b), 4(d), and 4(f), respectively.

As shown in Fig. 12(a), when $k = 0.5$, the phase difference $\Delta\theta(t)$ initially oscillates but eventually converges to a constant value, indicating the occurrence of phase synchronization. In Fig. 12(b), for $k = 1.1$, the system is initially asynchronous but then transitions into phase synchronization. In contrast, Fig. 12(c) shows that when $k = 1.7$, the phase difference remains in persistent fluctuation, reflecting asynchronization. Nonetheless, these fluctuations are bounded within a finite range.

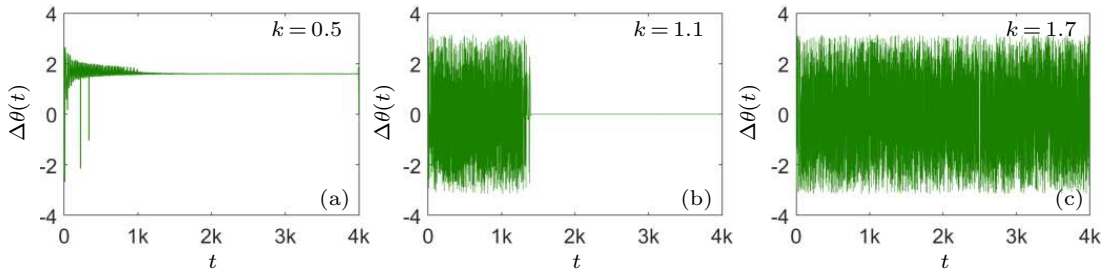


Fig. 12. Time sequences of the phase difference $\Delta\theta(t)$ between x_1 and x_3 for different coupling strengths k, with initial states (2, 0, 0, 0, 0). (a) Phase synchronization at $k = 0.5$; (b) partial phase synchronization at $k = 1.1$; (c) asynchronization at $k = 1.7$.

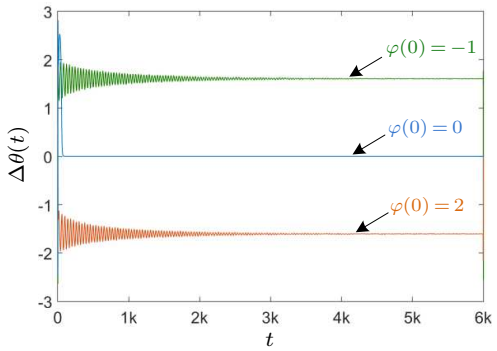


Fig. 13. Time sequences of the phase difference $\Delta\theta(t)$ between x_1 and x_3 for $k = 0.3$ with initial states (2, 0, 0, 0, $\varphi(0)$). The curves correspond to $\varphi(0) = -1$ (green), $\varphi(0) = 0$ (blue), and $\varphi(0) = 2$ (orange).

For different memristor initial values $\varphi(0)$, the time sequences of the phase difference $\Delta\theta(t)$ are presented in Fig. 13 for $k = 0.3$. As observed, phase synchronization occurs when $\varphi(0) = -1$, 0, and 2. In particular, for $\varphi(0) = 0$, the system converges rapidly to zero. In contrast, when $\varphi(0) = -1$ or 2, the system initially exhibits oscillatory behavior before gradually approaching a steady constant value, indicating a transient synchronization process. Notably, the final synchronized phase difference depends on the initial value of $\varphi(0)$, resulting in parallel offset states in the asymptotic regime.

5. FPGA-based hardware implementation

Analog circuits are often affected by parasitic parameters, temperature drift, and other environmental factors. To overcome these limitations, this study implements the MB-HNN model on an FPGA platform, leveraging its flexible architecture and high-speed parallel processing capabilities.[57] The FPGA implementation uses the XC7Z020-CLG400 chip to experimentally verify the numerical simulation results.

System (3) is discretized using the fourth-order Runge–Kutta scheme, and a 32-bit floating-point format is adopted to ensure high-precision computation. The discrete system is implemented in VHDL and downloaded to the FPGA chip, whose output is interfaced with a 14-bit DAC (AN9767). The resulting output waveforms are recorded using a four-channel digital oscilloscope. The experimental prototype of the FPGA-

based hardware platform is illustrated in Fig. 14.

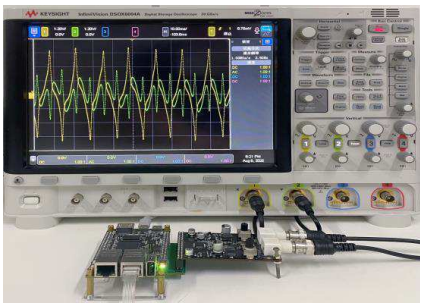


Fig. 14. FPGA-based hardware implementation of the MB-HNN.

For $\varphi(0) = 0$, $\pm 2\pi$, and $\pm 4\pi$, the system parameters from the numerical simulations in Fig. 6 are preloaded into the FPGA platform, with the four neuron initial states set as $(x_1(0), x_2(0), x_3(0), x_4(0)) = (2, 0, 0, 0)$ and coupling strength $k = 1.8$. The phase portraits of the resulting attractors for these five initial values are presented in Fig. 15. Each portrait was independently captured using the digital oscilloscope and subsequently combined into a single figure using Adobe Photoshop. The experimental results confirm the initial-offset coexisting behaviors observed in the numerical simulations.

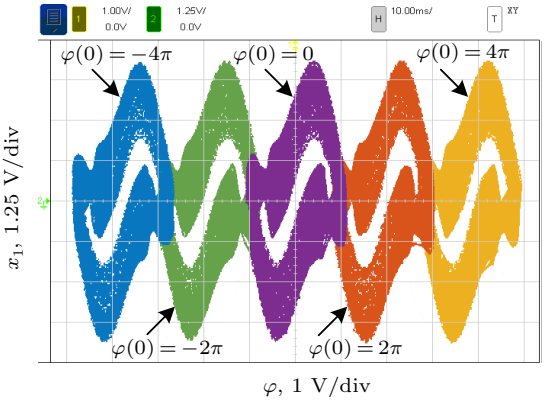


Fig. 15. Experimentally measured phase portraits of initial offset coexisting attractors in the φ–x_1 plane for $\varphi(0) = 0, \pm 2\pi, \pm 4\pi$ with $k = 1.8$.

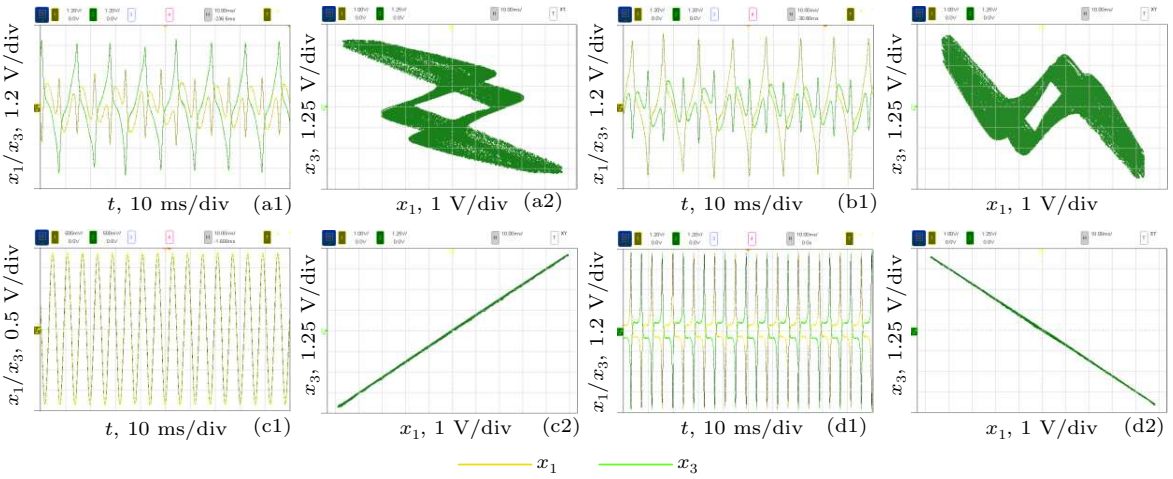


Fig. 16. Experimentally measured synchronous behaviors for different k and $\varphi(0)$ under four neuron initial states (2, 0, 0, 0), where (a1)–(d1) are the time sequences of periodic or chaotic firing, and (a2)–(d2) are the phase portraits on the x_1–x_3 plane. (a) $k = 1.6$, $\varphi(0) = 0$; (b) $k = 1.6$, $\varphi(0) = 0.5$; (c) $k = 1$, $\varphi(0) = 1$; (d) $k = 2.3$, $\varphi(0) = 1$.

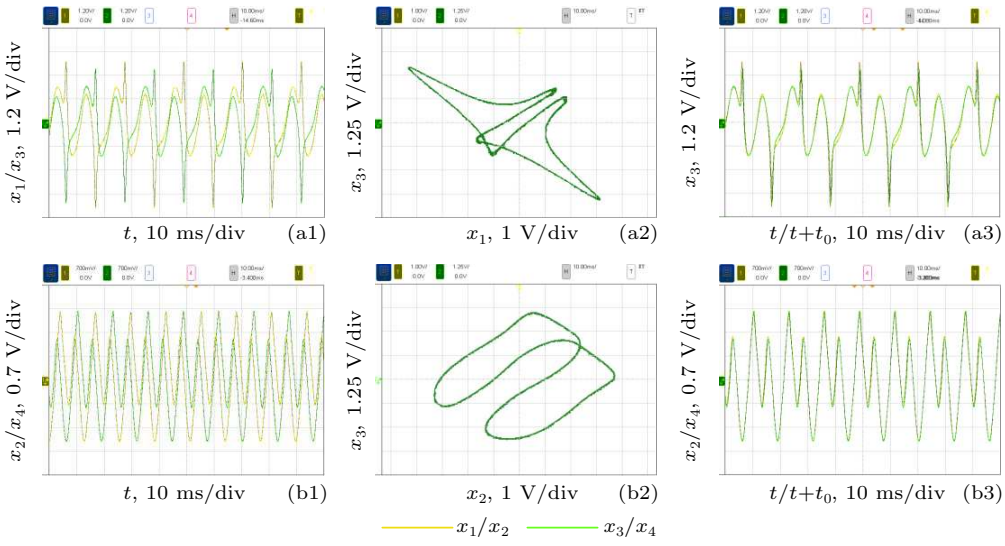


Fig. 17. Experimentally measured lag synchronization behaviors for $k = 1.9$ and initial states (2, 0, 0, 0, 0), where (a1), (a3), (b1), and (b3) are the time sequences of firing, and (a2) and (b2) are the phase portraits on the x_1–x_3 and x_2–x_4 planes, respectively. (a) Trajectories of x_1 and x_3; (b) trajectories of x_2 and x_4.

The synchronous behaviors shown in Fig. 8 were experimentally reproduced using identical system parameters and neuron initial states for several combinations of k and $\varphi(0)$. The experimentally obtained time sequences and phase portraits, presented in Fig. 16, closely match the numerical results, demonstrating the consistency between the hardware implementation and the simulations.

Furthermore, to experimentally realize the lag synchronization behaviors depicted in Fig. 11, the coupling strength and initial states were set to $k = 1.9$ and $(x_1(0), x_2(0), x_3(0), x_4(0), \varphi(0)) = (2, 0, 0, 0, 0)$. The experimentally measured time sequences and phase portraits, shown in Fig. 17, are in close agreement with the numerical results, thereby validating the hardware implementation of lag synchronization.

In summary, the FPGA-based experimental results exhibit strong consistency with the numerical simulations for both dynamical behaviors and synchronization in the coupled system, confirming the accuracy of the numerical analysis.

6. Conclusions

In this paper, a MB-HNN model was constructed and analyzed. While each individual bi-neuron module, as the lowest-dimensional HNN, cannot generate chaos, memristive coupling induces rich dynamical behaviors. The system possesses an unstable line of equilibria along the φ-axis and exhibits abundant dynamics, including initial-offset-regulated multistability.

Synchronization analysis identified complete, inverse, lag, and phase regimes, with transitions highly dependent on coupling strength and the initial state of the memristor. This dependence suggests a neuromorphic analogy, where perturbations to connectivity or instantaneous neural states in biological systems may promote synchronization linked to neurological disorders. Real-time FPGA experiments confirmed the predicted behaviors, establishing memristive coupling as a compact yet powerful approach for generating and controlling complex neural dynamics, with relevance to nonlinear science, neuromorphic hardware, and brain-inspired synchronization research.

Acknowledgments

This work was supported by the National Natural Science Foundation of China (Grant No. 62271088), the Qinglan Project of Jiangsu Province, and the Jiangsu Government Scholarship for Overseas Studies, the Training Plan of Young Backbone Teachers in Universities of Henan Province (Grant No. 2023GGJS142), and the Key Scientific Research of Colleges and Universities in Henan Province (Grant No. 25A120009).

References

[1] Korn H and Faure P 2003 *Comptes Rendus Biologies* **326** 787
[2] McKenna T M, McMullen T A and Shlesinger M F 1994 *Neuroscience* **60** 587
[3] Thottil S K and Ignatius R P 2017 *Nonlinear Dyn.* **87** 1879
[4] Wu H G, Gu J X, Wang N, Chen M and Xu Q 2025 *Chaos Soliton Fractals* **192** 115969
[5] Du S C, Zhang Z D, Li J, Sun C, Sun J R and Hong Q H 2024 *IEEE Trans. Biomed. Circuits Syst.* **17** 433
[6] Hopfield J J 1984 *Proc. Natl. Acad. Sci. USA* **81** 3088
[7] Hu J Y C, Wu D and Liu H 2024 *Adv. Neural Inf. Process. Syst.* **37** 70693
[8] Rbihou S, Joudar N E and Haddouch K 2024 *Ann. Math. Artif. Intell.* **92** 257
[9] Li X X, He Q Q, Yu T Y, Cai Z and Xu G Z 2024 *Chin. Phys. B* **33** 030505
[10] Feng B S and Liu Z Y 2025 *Nonlinear Dyn.* **113** 23521
[11] Ravi V 2025 *Phys. Scr.* **100** 035011
[12] Yu F, Zhang Z N, Shen H, Huang Y Y, Cai S and Du S C 2022 *Chin. Phys. B* **31** 020505
[13] Lai Q, Qin M H and Chen G R 2025 *Chaos Soliton Fractals* **199** 116663
[14] Li F Y, Chen Z G, Zhang Y Z, Bai L F and Bao B C 2024 *AEÜ-Int. J. Electron Commun.* **174** 155037
[15] Sporns O 2013 *NeuroImage* **80** 53
[16] Grover S, Nguyen J A and Reinhart R M 2021 *Annu. Rev. Med.* **72** 29
[17] Min F H, Chen C J and Broderick N G R 2025 *IEEE Trans. Neural Netw. Learn. Syst.* **36** 11632
[18] Zhou P, Ma J and Xu Y 2023 *Chaos Soliton Fractals* **169** 113238
[19] Wu F Q, Kang T, Shao Y and Wang Q Y 2023 *Chaos Soliton Fractals* **172** 113569
[20] Prodromakis T, Toumazou C and Chua L 2012 *Nat. Mater.* **11** 478
[21] Lanza M, Pazos S, Aguirre F, Sebastian A, Le Gallo M, Alam S M, Ikegawa S, Yang J J, Vianello E, Chang M F, Molas G, Naveh I, Ielmini D, Liu M and Roldan J B 2025 *Nature* **640** 613
[22] Song F M, Shao H, Ming J Y, Sun J T, Li W, Yi M D, Xie L H and Ling H F 2024 *Adv. Mater. Technol.* **9** 2400764
[23] Qin M H, Lai Q, Wang H T and W Z Q 2025 *Chaos* **35** 023123
[24] Ma Q Q, Lu A J and Huang Z 2024 *Chin. Phys. B* **33** 120502
[25] Yang F F, Ma J and Wu F Q 2024 *Chaos Soliton Fractals* **187** 115361
[26] Yu X H, Bao H, Xu Q, Chen M and Bao B C 2024 *Neural Netw.* **180** 106728
[27] Biamou A L M, Tamba V K, Tagne F K and Takougang A C N 2024 *Chaos Soliton Fractals* **178** 114267
[28] Sun J W, Li C C, Wang Z C and Wang Y F 2023 *Appl. Math. Model* **121** 463
[29] Ding D W, Niu Y, Zhang H W, Yang Z L, Wang J, Wang W and Wang M Y 2024 *Chin. Phys. B* **33** 050503
[30] Lin H R, Wang C H, Li C, Sun Y C, Xu C and Yu F 2022 *IEEE Trans. Ind. Informat.* **18** 8839
[31] Bao H, Li K X, Ma J, Hua Z Y, Xu Q, and Bao B C 2023 *Sci. China Technol. Sci.* **66** 3153
[32] Ma T, Mou J, Al-Barakati A, Jahanshahi H and Miao M 2023 *Phys. Scr.* **98** 105202
[33] Ma M M, Xiong K L, Li Z J and He S B 2024 *Chin. Phys. B* **33** 028706
[34] Chen M, Luo X F, Suo Y H, Xu Q and Wu H G 2023 *Nonlinear Dyn.* **111** 7773
[35] Njitacke Z T, Awrejcewicz J, Telem A N K, Fozin T F and Kengne J 2023 *IEEE Trans. Circuits Syst. II, Exp. Briefs* **70** 791
[36] Wang C H, Tang D, Lin H R, Yu F and Sun Y C 2024 *Expert. Syst. Appl.* **242** 122513
[37] Chen M, Zhang Y C, Wu H G and Xu Q 2025 *IEEE Trans. Circuits Syst. I, Reg. Pap.* **72** 6914
[38] Li Z J, Li Z, He S B, Wang H H and Wu X M 2025 *Eur. Phys. J. Spec. Top.*
[39] Boccaletti S, Kurths J, Osipov G, Valladares D L and Zhou C S 2002 *Phys. Rep.* **366** 1
[40] Kim C H, Park J, Kim Y J, Park S, Boccaletti S and Kahng B 2025 *Chaos Soliton Fractals* **196** 116281
[41] Jiruska P, Curtis M, Jefferys J G, Schevon C A, Schiff S J and Schindler K 2013 *J. Physiol.* **591** 787
[42] Ding D W, Chen S Q, Yang Z L, Xu X Y, Fan J, Zhu H F and Liu X 2025 *Cogn. Neurodyn.* **19** 102

[43] Shang C X, Sun K H, Wang H H, Yao Z and He S B 2023 *Nonlinear Dyn.* **111** 20347
[44] Li C L, Wang X, Du J R and Li Z J 2023 *Nonlinear Dyn.* **111** 21333
[45] Bao B C, Hu J T, Bao H, Xu Q and Chen M 2024 *Cogn. Neurodyn.* **18** 539
[46] Wang Z, Parastesh F, Rajagopal K, Hamarash I I and Hussain I 2020 *Chaos Soliton Fractals* **134** 109702
[47] Boya B F B A, Muni S S, Echenausía-Monroy J L and Kengne J 2025 *Eur. Phys. J. Spec. Top.* **234** 1735
[48] Chen C J, Bao H, Zhang Y Z, Yu Y, Zhao S and Yang Y 2025 *IEEE Trans. Circuits Syst. I, Reg. Pap.* **72** 4854
[49] Li F Y, Chen Z G, Bao H, Bai L F and Bao B C 2024 *Chaos Soliton Fractals* **184** 115046
[50] Li F Y, Bai L F, Chen Z G and Bao B C 2024 *IEEE Trans. Circuits Syst. II, Exp. Briefs* **71** 2354
[51] Ma J 2025 *Nonlinear Dyn.* **113** 25365
[52] Gu Y, Bao H, Yu X H, Hua Z Y, Bao B C and Xu Q 2024 *Sci. China Technol. Sci.* **67** 1855
[53] Zhao Q H, Bao H, Zhang X, Wu H G and Bao B C 2025 *Nonlinear Dyn.* **113** 2747
[54] Rosenblum M G, Pikovsky A S and Kurths J 1997 *Phys. Rev. Lett.* **78** 4193
[55] Li Z J, Zhou H Y, Wang M J and Ma M L 2021 *Nonlinear Dyn.* **104** 1455
[56] Chen X J, Wang N, Wang K, Chen M, Parastesh F and Xu Q 2024 *Nonlinear Dyn.* **112** 20365
[57] Bao H, Xi M Q, Tang H G, Zhang X, Xu Q and Bao B C 2024 *IEEE Trans. Ind. Inf.* **21** 1862